

# Building Self-Consistent Triaxial Galaxy Models Using Schwarzschild's Method

Balša Terzić

*Mathematics Department, Florida State University, Tallahassee, FL 32306*

*Astronomy Department, University of Florida, Gainesville, FL 32611*

bterzic@astro.ufl.edu

## ABSTRACT

We use Schwarzschild's orbit superposition method to build self-consistent models of elliptical galaxies with scale-free potentials. Our exhaustive study of all physical shapes and central densities for galaxies with scale-free potentials establishes a relationship between the presence of chaos and self-consistency. The extent and the onset of chaos is studied by varying parameters of the model which are believed to be its inducers, such as the steepness of the central density cusp, flatness and triaxiality. We show that gravitational scattering of the central density cusp plays a dominant role in restricting the shapes of elliptical galaxies.

*Subject headings:* celestial mechanics — stellar dynamics — galaxies: kinematics and dynamics — galaxies: elliptical and lenticular, CD

## 1. Introduction

Recent observational data has shown that most, if not all, elliptical galaxies feature power-law density distributions which rise into the smallest observable radii, thus causing them to have central density cusps (Crane et al. 1993; Moller, Stiavelli & Zeilinger 1995; Lauer et al. 1995; Gebhardt et al. 1996). Inner parts of most of these galaxies have two power-law regimes, with the core radius being the boundary between the steep outer and shallow inner density profiles (Gebhardt et al. 1996). Some, however, seem to obey one uniform power-law throughout, thus rendering them scale-free. It is also important to note that orbits in the outer parts of galaxies with two power-law regimes as well as the ones quite close to the center are essentially scale-free because of their distance from the core. These reasons, along with the fact that a great deal of simplification is introduced in studying this family of potentials, make scale-free models of great interest.

It has long been speculated that a presence of a black hole or a central density cusps may disrupt most box orbits and thus cause a loss of triaxi-

ality in the innermost parts (Gerhard & Binney 1985). Our goal is to study the dependence of the model's self-consistency on the strength of its central density cusp, as well as its flattening and triaxiality. In order to foster a thorough and comprehensive investigation of this dependence, our models span the entire ranges of elongation and central density observed in nature, while varying triaxiality from one physical extreme to the other. Photometric observations of elliptical galaxies reveal that they range from spherical  $E0$  to quite elongated  $E6$ , whose ratio of lengths of short to long axis is  $c/a = 0.4$ . High resolution HST observations, which peer into the very centers of elliptical galaxies, reveal that the galactic density profiles rise as power-laws  $\rho \sim r^{-\gamma}$  as the center is approached, with the strength of the central cusp being in the range  $\gamma = [0.25, 2]$  (Lauer et al. 1995).

Schwarzschild's method has been a traditional tool for probing the dynamics of elliptical galaxies. It was applied to a number of axisymmetric and disky (Cretton et al. 1999; Verolme & de Zeeuw 2002; Jalali & de Zeeuw 2002), as well as triaxial potentials, both integrable (Statler 1987; Siopis 1999) and non-integrable (Schwarzschild

1979, 1993; Merritt & Fridman 1996; Siopis 1999). Earlier applications of Schwarzschild’s method to triaxial systems either studied models of one or two particular density profiles and varying galactic shapes (Statler 1987; Schwarzschild 1993; Merritt 1997; Poon & Merritt 2001), or have investigated a range of density profiles for fixed galactic shapes (Merritt & Fridman 1996; Siopis 1999). Our study provides the most exhaustive coverage of *both* density profiles and galactic shapes, spanning virtually the entire range of physically plausible models for galaxies with scale-free potentials and singular central densities. This enables us to better understand the dependence of models’ self-consistency on these properties. By investigating orbits in scale-free potentials, we single out the effects of power-law central density singularities on their stability. Our models present a useful tool for studying the stability and self-consistency of triaxial elliptical galaxies with central density cusps. In §2, we outline the extent of our study and review major properties of scale-free potentials. §3 covers major issues in the numerical implementation of Schwarzschild’s method. Major findings of the study are reported in §4 and their significance and impact discussed in §5.

## 2. Mass Models

We investigate scale-free models for which the isodensity surfaces are similar concentric ellipsoids. Their densities are given by the power-law formula

$$\rho = \rho_0 m^{-\gamma}, \quad (1)$$

where

$$m^2 = \frac{x^2}{a^2} + \frac{y^2}{b^2} + \frac{z^2}{c^2}. \quad (2)$$

We take  $a$ ,  $b$  and  $c$  to be the long, intermediate, and short axes respectively. To simplify the computations of forces, we represent the density by the double expansion

$$\rho(r, \theta, \phi) = r^{-\gamma} \sum_{m=0}^{M_{\max}} \sum_{n=m}^{M_{\max}} D_{mn} \cos 2m\phi P_{2n}^{2m}(\cos \theta), \quad (3)$$

in the usual spherical coordinates of radial distance  $r$ , azimuthal angle  $\phi$ , and polar angle  $\theta$  (Binney & Tremaine 1987). Here  $P_{2n}^{2m}$  is an associated Legendre function. The special form of this expansion is due to the eight-fold symmetry of the

density which is even in  $x$ ,  $y$ , and  $z$ . The potential is found from Poisson’s equation as

$$\Phi(r, \theta, \phi) = r^{2-\gamma} \sum_{m=0}^{M_{\max}} \sum_{n=m}^{M_{\max}} C_{mn} \cos 2m\phi P_{2n}^{2m}(\cos \theta), \quad (4)$$

for  $\gamma \in [0, 2)$ , and

$$\begin{aligned} \Phi(r, \theta, \phi) &= \sum_{m=0}^{M_{\max}} \sum_{n=m}^{M_{\max}} C_{mn} \cos 2m\phi P_{2n}^{2m}(\cos \theta) \\ &+ 4\pi G D_{00} \ln r, \end{aligned} \quad (5)$$

for  $\gamma = 2$ . Except for the special case of  $\gamma = 2$  and  $m = n = 0$ , the coefficients of the two expansions are related by the formula

$$D_{mn} = \frac{C_{mn}}{4\pi G} [(2-\gamma)(3-\gamma) - 2n(2n+1)]. \quad (6)$$

The coefficients of the expansion for the density are given by

$$\begin{aligned} D_{mn} &= \frac{2\rho_0(2-\delta_{m0})(4n+1)(2n-2m)!}{\pi(2n+2m)!} \\ &\times \int_0^{\pi/2} d\phi \cos 2m\phi \\ &\times \int_0^1 d\mu \left[ \frac{\mu^2}{c^2} + (1-\mu^2)q \right]^{-\gamma/2} P_{2n}^{2m}(\mu), \\ q &= \left( \frac{\cos^2 \phi}{a^2} + \frac{\sin^2 \phi}{b^2} \right) \end{aligned} \quad (7)$$

where  $\delta_{m0}$  is a Kronecker delta which is unity for  $m = 0$  but zero otherwise. Even with  $M_{\max} = 4$ , the truncated Fourier–Legendre expansions (4) and (5) for the potential are accurate to within  $10^{-4}$ , while expansion (3) for the density is accurate to within 1% even for the most flattened models.

## 3. Numerical Implementation

Our computations made use of the IBM RS/6000 SP supercomputer at the Florida State University School of Computational Science and Information Technology. It features 42 4-way 375 MHz Power 3 nodes. Parallel programming and aggressive compiler optimization resulted in twenty- to thirty-fold increases in speed from the more conventional serial runs on Ultra Sparc UNIX workstations.

Orbit integrations used the DOP853 integration routine, the explicit imbedded (7,8) pair of

Dormand and Prince (Hairer, Norsett & Wanner 1993). It proved to be quite efficient in generating large number of orbital points needed for the frequency analysis. The errors in the energy conservation as well as the numerical integration have been on the order of  $10^{-8}$  even after hundreds of dynamical times.

### 3.1. Sampling the Phase Space

In order to assemble a library of orbits which is representative of all orbits in a given potential and without missing any major orbital families, the phase space must be systematically sampled. Schwarzschild (1993) proposed a two-fold 2-D start-space; *the stationary start-space* contains initial conditions starting from equipotential surfaces with zero velocities, while *the principal-plane start-space* features radially stratified initial conditions which pierce one of the three principal planes with the velocity vector normal to the plane. These spaces are designed to pick up different kinds of orbits arising in triaxial potentials; stationary start-space picks up orbits which have zero-velocity turning points, such as boxes and resonant boxlets, while the principal-plane start-space selects mostly tube orbits. It is probable, yet not certain, that the combination of these two start-spaces covers all the phase space of triaxial potentials (Schwarzschild 1993). In any case, it is necessary to understand which orbital structures are represented in such spaces, as well as determine which ones are likely to be left out (cf. Appendix A).

We integrate 2304 orbits from the stationary start-space, by placing 12 equally spaced initial conditions in each of the 192 cells of the reference sphere (cf. §3.4.1). A total of 1000 orbits with the same energy are sampled on each principal plane, spanning an elliptical annulus with an outer radius equal to the radius of the equipotential surface. The inner boundary of the annulus in each of the planes is chosen to be an ellipse whose axes are radii of the periodic 1:1 thin tube orbits perpendicular to that plane. This ensures that the innermost initial conditions from the principal plane start space correspond to thin tubes. In all, a total of 5304 initial conditions is integrated for each model (Figure 1). Each orbit is integrated for 200 dynamical times, which we define to be the maximum of the periods of thin tubes in three

principal planes.

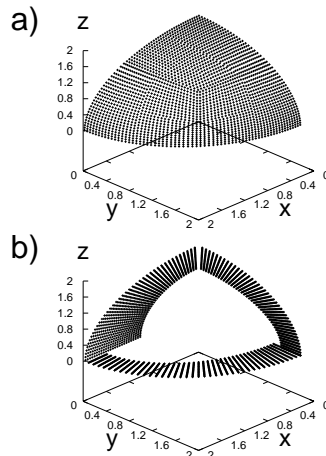


Fig. 1.— Initial condition spaces: a) stationary start-space b) principal-plane start-space.

### 3.2. Orbital Structure

We classify orbits based on the resonances between leading frequencies in the Cartesian coordinates (LFCCs), and follow the paradigm given in the Table 1 of (Schwarzschild 1993). The most dominant families are boxes, short axis tubes (S-tubes), inner long axis tubes (I-tubes), outer long axis tubes (O-tubes) and resonant boxlets. The LFCCs of the boxes are all distinct; tube orbits, however, have the same LFCCs in coordinates normal to their axis of rotation. For the resonant orbits, the ratio of LFCCs in two or more coordinates is a ratio of integers. Low order resonances, the ones for which the ratio of LFCCs is a ratio of small integers, occupy a larger portion of the phase space than the high-order resonant families (cf. Appendix A). This classification enables us to utilize the ratio of LFCCs space in analyzing populations of orbits.

Two initial condition spaces provide two distinct orbital populations. Stationary start-space yields mainly resonant orbits (boxlets) or unstable boxes, while the principal-plane start-space produces mostly tubes. This duality is evident in

the graphs of the ratios of LFCCs. Note that the fundamental frequencies do not necessarily correspond to LFCCs; the two are equivalent for box orbits and other resonant orbits, but the tube orbits have three distinct fundamental frequencies, while having the same LFCCs normal to the axis of revolution. This loss of information does not hurt our purposes; using LFCCs to classify orbits, measure chaotic diffusion and demonstrate duality of the two initial condition spaces is equivalent and just as effective as using fundamental frequencies. Figure 2 shows the locations of orbits for each of the two start-spaces in the ratio of frequencies space. In the ratio of frequencies space, tubes are concentrated around lines  $\nu_x/\nu_z = \nu_y/\nu_z$  (S-tubes) and  $\nu_y/\nu_z = 1$  (I- and O-tubes), which is indeed where most of the orbits from the principal-plane start-space are concentrated. Resonant orbits and boxes occupy a region between these lines, where a number of resonant lines intersect. Some overlap between the two spaces is to be expected, since neither can exclusively pick up only one population of orbits. It is particularly interesting to look at the transition from prolate to oblate models. For prolate models, all orbits are I- or O-tubes, located along the line  $\nu_y/\nu_z = 1$ , but as the triaxiality decreases and the models become more oblate, orbits in both spaces seem to shift steadily toward the S-tubes (line  $\nu_x/\nu_z = \nu_y/\nu_z$ ) until they completely align with it for oblate models. Our earlier studies of 2D oblate and prolate scale-free models revealed very little chaos (Hunter et al. 1998), which is consistent with Figure 2. The bottom row shows the fraction of regular orbits as a function of the chaotic diffusion parameter  $\omega$ , as defined in (9).

### 3.3. Detecting Chaotic Orbits

Chaotic orbits are not time-independent – their orbital properties, such as eccentricity, radial excursion and orbital densities, evolve in time. In three degrees of freedom systems, all chaotic portions of the phase space are interconnected (Arnold’s web), so that every chaotic orbit will eventually visit each chaotic section. Thus, we may choose to look at each of the chaotic orbits as different parts of *one* chaotic ‘super-orbit’. This super-orbit gives the averaged density of the stochastic portions of the phase space, and therefore is time-independent. If orbit integration is

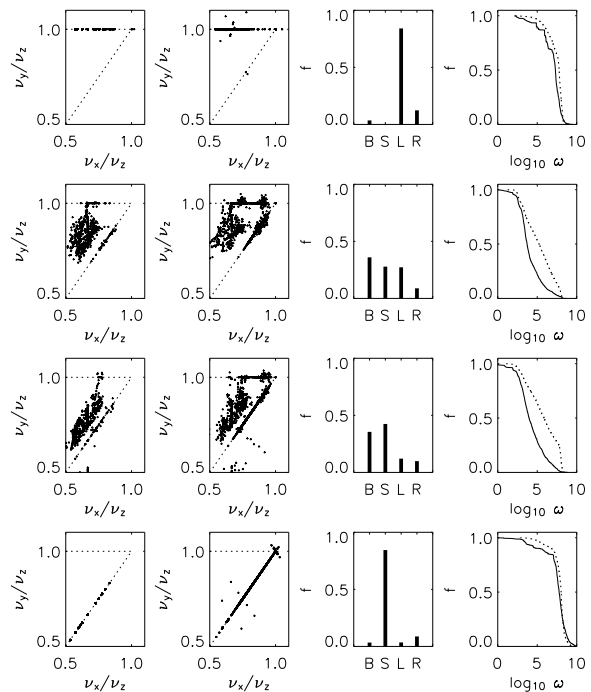


Fig. 2.— Ratios of leading frequencies in Cartesian coordinates for the stationary start-space (first column) and principal-plane start-space (second column) for (top to bottom) T=1 (prolate), T=0.7 T=0.3 and T=0.0 (oblate). The third column shows the fraction of orbits in each of the four major orbital families: B - boxes, S - short axis tubes, L - long axis tubes, R - resonant orbits. The fourth column shows the fraction of orbits with the diffusion parameter greater than  $\omega$ .

carried over sufficiently long time intervals, then the time-averaged orbital density of each chaotic orbit would approximate the density of the chaotic super-orbit. However, the integration interval required for achieving a good time-averaged approximation may be quite long for some weakly chaotic orbits residing near the boundary between chaotic and regular portions of the phase space, thus rendering this approach numerically impractical. It is more efficient to take a simple arithmetic average of orbital densities of *all* chaotic orbits of the model to get a more accurate representation of the chaotic super-orbit (Merritt & Fridman 1996). We are looking for true equilibrium solutions, and therefore only include time independent building blocks into Schwarzschild’s method: regular orbits and *one* chaotic super-orbit. This necessitates careful distinction between chaotic and regular orbits.

Both regular orbits and the chaotic super-orbit can be viewed as ergodic – they sample all of the allowed phase space. A major difference between the two is that the phase-space volume occupied by the chaotic orbits is much larger, thus making it impossible to represent it accurately with just one orbital ‘snapshot’ obtained after a finite integration of a single orbit. The size of the phase-space volume of the stochastic region enables vast numbers of these different orbital snapshots of a same super-orbit to exist. Therefore, in order to have a good approximation to the contribution of the stochastic orbits to the model’s density, we combine the information conveyed in the individual snapshots into a *single* chaotic super-orbit.

We use Hunter’s method (Hunter 2002) to compute the diffusion in fundamental frequencies (FFs) of an orbit integrated over two consecutive time intervals. The method extracts frequencies from an orbit given in the form of a time series. We have discovered that Hunter’s method is more accurate and more efficient than Laskar’s numerical analysis of fundamental frequencies method (Laskar et al. 1992; Laskar 1993) by a few orders of magnitude. This is because it relies entirely on discrete Fourier transforms. All of the extracted frequencies will be linear combinations of three FFs. These FFs will remain constant if the motion is regular. When the motion is chaotic, these FFs will change. The relative rate of change in FFs of an orbit over the integration interval is

the measure of its averaged stochasticity over that time span. We compute the norm of the diffusion in the leading frequencies in Cartesian coordinates, instead of the norm of the diffusion in the fundamental frequencies. The two are equivalent, since frequencies in Cartesian coordinates are linear combinations of the fundamental frequencies.

We seek to compute the average stochasticity of an orbit over a certain finite time interval. The average rate of diffusion in FFs is computed for each orbit over an integration interval  $t = [0, 2T]$ , where  $2T$  corresponds to  $n_d = 200$  dynamical times. We use these rates of diffusion to compute how many crossings it would, at that rate, take for a particular orbit to ‘lose memory’ of its initial FFs, i.e. become relaxed. More precisely, if we measure the FFs over two consecutive time intervals  $t_1 = [0, T]$  and  $t_2 = [T, 2T]$  to be  $\mathbf{\Omega}_1$  and  $\mathbf{\Omega}_2$ , the average diffusion rate of FFs over the time interval  $[0, 2T]$  is

$$\delta\mathbf{\Omega} = \frac{|\mathbf{\Omega}_1 - \mathbf{\Omega}_2|}{T}. \quad (8)$$

We define an orbit to be relaxed when the change in FFs is on the order of the FFs themselves. At the rate of diffusion of  $\delta\mathbf{\Omega}$ , this corresponds to the number

$$\omega = \frac{|\delta\mathbf{\Omega}|}{|\mathbf{\Omega}_1|} n_d. \quad (9)$$

of crossings (or dynamical times). Measuring diffusion in FFs is equivalent to computing short time Lyapunov exponents, since both measure an orbit’s average orbital stochasticity over a finite time interval.

The scale-free potentials do not have an intrinsic time/length scale associated with them. This requires our criterion for determining an orbit’s stochasticity to be tied in with the number of crossings of an orbit instead of some absolute time interval, such as the Hubble time. We define  $\omega$  to be the number of crossings it takes for an orbit to become fully relaxed. We adopt a convention that an orbit is chaotic if the full relaxation is expected to set in within  $10^4$  crossings ( $\log_{10} \omega = 4$ ). Considering that the number of crossings a typical orbit of an elliptical galaxy has gone through is between 20-50 for the ones in the outer parts and a few hundred for the ones near the center, this seems like a reasonable cut-off point. We discuss the effects of varying this stochasticity criterion in §4.1.

As the chaotic threshold is increased, more orbits are labeled as chaotic and included into a super-orbit. In theory, averaging over all chaotic orbits will approximate the phase-space density of the interconnected chaotic sea, with its accuracy increasing as with the increase in the number of stochastic orbits and the length of the integration time. In practice, however, the integration time is finite, and the weakly chaotic orbits may only sample a limited region of the phase space, which may lead to a super-orbit which is not entirely time-independent. Possible time-dependence of the super-orbit is of little practical significance, since we find that including the super-orbit, as opposed to not including it, will never change model's self-consistency. This is the consequence of the fact that the super-orbit is an average of an ensemble of many nearly-ergodic orbital densities, which make its orbital density round and, as such, not crucial for reproducing the desired galaxy shapes.

### 3.4. Constructing Self-consistent Scale-Free Models

#### 3.4.1. Coarse-graining of the Configuration Space

The advantage of using a scale-free potential with triaxial symmetry is that one needs to consider only an octant of a 2-D *reference sphere* ( $r = R_{\text{ref}}$ ) (Richstone 1980; Schwarzschild 1993). Each orbit produces a *template* orbital density which represents an ensemble of geometrically similar orbits. For any orbit through a point at radial distance  $r$ , there will be a geometrically similar orbit which passes through the reference sphere whose length scale differs by a factor  $R_{\text{ref}}/r$ . With density proportional to  $r^{-\gamma}$ , it follows that we should give each orbital point on a computed orbit the weight  $(r/R_{\text{ref}})^{\gamma-3}$  (Richstone 1980; Schwarzschild 1993).

Following Schwarzschild (1993), we consider only a positive octant of the reference sphere, which we divide into 3 regions with planes  $x = y$ ,  $x = z$ , and  $y = z$ , so that Region 1 is the one with  $x > y$ ,  $x > z$ , Region 2 with  $y > x$ ,  $y > z$  and Region 3 with  $z > x$ ,  $z > y$ . Each region is then subdivided into 64 parts of equal surface area as follows. We first divide Region 1 into two equal halves with a vertical line  $v \equiv y/x = v_i$ , and then split each half in two with two horizon-

	$h$	$v$
Region 1	$h_{\min} \leq \frac{z}{x} \leq h_{\max}$	$v_{\min} \leq \frac{y}{x} \leq v_{\max}$
Region 2	$h_{\min} \leq \frac{z}{y} \leq h_{\max}$	$v_{\min} \leq \frac{x}{y} \leq v_{\max}$
Region 3	$h_{\min} \leq \frac{y}{z} \leq h_{\max}$	$v_{\min} \leq \frac{x}{z} \leq v_{\max}$
	$\phi_{\min}$	$\phi_{\max}$
Region 1	$\tan^{-1} \frac{1}{v_{\min}}$	$\tan^{-1} \frac{1}{v_{\max}}$
Region 2	$\tan^{-1} \frac{1}{v_{\max}}$	$\tan^{-1} \frac{1}{v_{\min}}$
Region 3	$\tan^{-1} \frac{h_{\min}}{v_{\max}}$	$\tan^{-1} \frac{h_{\max}}{v_{\min}}$
	$\theta_{\min}$	$\theta_{\max}$
Region 1	$\tan^{-1} \frac{1}{h_{\max} \cos \phi}$	$\tan^{-1} \frac{1}{h_{\min} \cos \phi}$
Region 2	$\tan^{-1} \frac{1}{h_{\max} \sin \phi}$	$\tan^{-1} \frac{1}{h_{\min} \sin \phi}$
Region 3	$\tan^{-1} \frac{h_{\min}}{\sin \phi}$	$\tan^{-1} \frac{h_{\max}}{\sin \phi}$

Table 1: Limits of integration for each of the cells on the reference sphere.

tal lines  $h \equiv z/x = l_i$  and  $h = r_i$ . This step yields four parts of equal surface area, and can be recursively applied to each partition; in  $n$  such recursive steps, the region can be divided into  $4^n$  cells of equal area. We repeat this process until the region is split in 64 equal parts. Similar partitioning is done for the other two regions by rotating coordinates  $(x, y, z) \rightarrow (y, x, z)$  for Region 2, and  $(x, y, z) \rightarrow (z, x, y)$  for Region 3. We use a Maple program to carry out the relatively straightforward integral computations involved in finding the positions of the vertical and horizontal dividing lines, i.e. the values of  $v_i$ ,  $l_i$  and  $r_i$ . Figure 3 shows the entire equipartitioned octant. Schwarzschild (1993) uses cells that are different in area to within few percent. Even though the equipartitioning of the reference sphere is not one of the key issues in the implementation of the Schwarzschild's method, it is, nonetheless, noteworthy that the algorithm outlined above achieves maximal accuracy with the same amount of work.

#### 3.4.2. Computing Model Mass in Cells

We compute surface mass on the reference sphere by integrating the density (3) over  $r = R_{\text{ref}} = 1$  to get

$$\begin{aligned}
 m_i &= \sum_{m=0}^{M_{\max}} \sum_{n=m}^{M_{\max}} D_{mn} \int_{\phi_{\min}}^{\phi_{\max}} d\phi \cos 2m\phi \\
 &\times \int_{\theta_{\min}}^{\theta_{\max}} d\theta \sin \theta P_{2n}^{2m}(\cos \theta), \quad (10)
 \end{aligned}$$

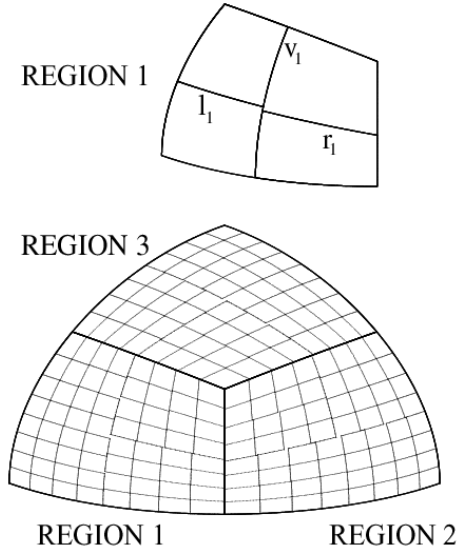


Fig. 3.— Equipartitioning of the reference sphere.

for the surface mass in the  $i$ -th cell. Each cell on the reference sphere is delimited by two constant values of each horizontal and vertical coordinates  $(h, v)$ , which, in turn, provide limits of integration for  $\phi$  and  $\theta$  (Table 1). The inner integrand is a polynomial of degree  $2n$  in  $\cos\theta$ , for which the Gaussian quadrature with  $2n$  points is exact.

### 3.4.3. Computing Orbital Mass in Cells

We need to be able to compute accurately the amount of time orbits spend in each of the cells of the reference sphere. When integrated for a fixed time interval, an orbit will generally not go through an integer number of crossings. In particular, if an orbit has  $n$  complete crossings in  $t$ , but  $t/n$  is not an integer, some parts of the orbit’s path will be sampled  $n + 1$  times, while others only  $n$  times. This will introduce a certain inaccuracy, which we minimize by increasing  $t$  in order to make  $n$  large. Orbits are given by a dense output of orbital points, which we further improve upon by linearly interpolating between them. We use an algorithm proposed by Siopis (1999); as long as consecutive orbital points are inside the same cell, advance orbital output in steps of  $t_0$ . When

the next orbital point is outside the current cell, the time is advanced in steps that are a factor of 10 and 100 smaller as the boundary between cells is approached. This algorithm ensures that the accuracy in determining the orbit’s contribution to the mass of each cell is computed to within  $0.01t_0$ .

### 3.4.4. Formulating the Optimization Problem

Schwarzschild’s method is formulated as an optimization problem:

$$\begin{aligned} \text{Minimize : } & f(w_i), \\ \text{Subject to : } & \sum_{i=1}^{N_o} w_i \rho_{ij} = \rho_j, \\ & w_i \geq 0, \end{aligned} \quad (11)$$

where  $j = 1, 2, \dots, N_c$ ,  $i = 1, 2, \dots, N_o$ ,  $f(w_i)$  is the cost function,  $\rho_{ij}$  is the contribution of the  $i$ th template to  $j$ th cell,  $\rho_j$  is the model’s density in the  $j$ th cell and  $w_i$  is the orbital weight of the  $i$ th orbit. This becomes a linear programming problem (LPP) when the cost function  $f$  is a linear function of the weights; for example, to minimize weights of orbits labeled from  $m$  to  $n$ , the cost function would simply be  $f(w_i) = \sum_{i=m}^n w_i$ . The solutions of the LPP are often quite noisy, with a significant number of orbits unpopulated (Siopis 1999). It is often customary to impose additional constraints in order to ‘smoothen’ out the solutions, such as minimizing the sum of squares of orbital weights, which makes this a quadratic programming problem, or minimizing the least squares. A thorough discussion of effects of this ‘smoothing’, as well as problems involving the formulation of the optimization problem, is given in Siopis (1999). Since our study focuses on establishing *existence* of self-consistent solutions, we solve only the LPP. We use the BPMPD (Mészáros 1996) routine, a primal-dual interior point algorithm for LPP. It features powerful pre-solve techniques, efficient sparsity handling, and flexible linear algebra. Each LPP of size  $N_o \times 192$ , where  $N_o \leq 5304$ , takes only a few seconds of CPU time on the RS/6000 SP.

In order to investigate how non-self-consistency sets in, it is advantageous to know which cells of the reference sphere are infeasible. We do this by reformulating the LPP above into another LPP which uses slack variables  $\lambda_i$  and  $\mu_i$  to make the

problem always feasible (Siopis 1999):

$$\begin{aligned} \text{Minimize : } & f(w_i) + p \sum_{j=1}^{N_c} (\lambda_j + \mu_j), \\ \text{Subject to : } & \lambda_j - \mu_j + \sum_{i=1}^{N_o} w_i \rho_{ij} = \rho_j, \quad (12) \\ & w_i, \lambda_j, \mu_j \geq 0, \end{aligned}$$

where  $j = 1, 2, \dots, N_c$ ,  $i = 1, 2, \dots, N_o$ , and  $p$ , the penalty parameter, is some positive constant. A self-consistent problem will have zero  $\lambda_j$  and  $\mu_j$ , while the deviation from exact self-consistency in non-self-consistent models can be traced by locating the non-vanishing values of the slack variables.

#### 4. Results

We study the set  $\gamma = \{0.5, 1, 1.5, 2\}$  of values of the central density cusp. For each  $\gamma$  we vary the elongation from  $c/a = 0.4$  to 1 in increments of 0.1. At each elongation, the triaxiality is varied through the *triaxiality parameter*  $T = (a^2 - b^2)/(a^2 - c^2)$ , from oblate ( $T = 0$ ) to prolate ( $T = 1$ ) in the interval  $T = \{0, 0.1, 0.3, 0.5, 0.7, 0.9, 1\}$ . Figure 4 plots the 42 different shapes we investigated in axis-ratio space. The hypotenuse of the triangle (line  $b = c$ ) represents prolate spheroids ( $T = 1$ ), the vertical side ( $b = a$  line) represents oblate spheroids ( $T = 0$ ), the vertex  $(1, 1)$  at which those two sides meet represents spherical models (Figure 4).

Only regular orbits and a single chaotic super-orbit (as an approximation to a time-independent phase space density of the chaotic portion of the phase space) are used in building self-consistent models using Schwarzschild’s method. Figure 5 shows the fraction of orbits from both stationary and principal-plane start-spaces, as a function of the degree of stochasticity  $\omega$  for models with weak and strong central cusps,  $\gamma = 0.5$  and  $\gamma = 2$  respectively. We note that the curves representing each of the start-spaces are relatively close together. As the strength of the cusp increases, the two lines move in opposite directions for non-axisymmetric cases ( $T \neq 0, 1$ ); the one representing the orbits from the stationary start-space drops off sooner and more abruptly, while the line corresponding to the principal-plane start-space becomes rounder, with its drop-off delayed.

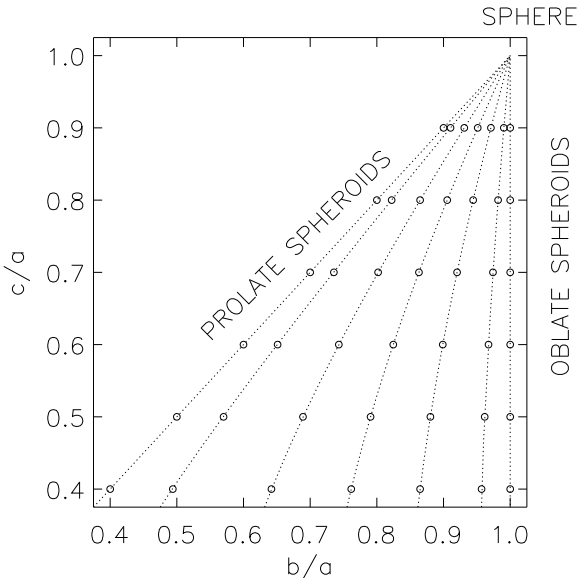


Fig. 4.— Axis ratio space: the stars represent models investigated. The lines connect points of equal triaxiality, from right to left,  $T = 0, 0.1, 0.3, 0.5, 0.7, 0.9, 1$ .

This clearly implies that increasing the strength of the central cusp has a destabilizing effect on orbits from the stationary start-space, which, as we established earlier, are mainly boxes and boxlets which pass near to the center. Increasing central mass concentration makes gravitational scattering of orbits more efficient, thus causing orbits to become more chaotic. Also, the tube orbits, which dominate the principal-plane start-space, are stabilized by the strengthening of the central cusp. They stay significantly away from the center, and therefore ‘see’ the central cusp as a point mass. The strengthening of the central cusp has the same effect on them as increasing the central point mass – it moves them toward a more Keplerian, integrable regime, causing them to be less chaotic. This behavior is more pronounced for the rounder models. In the absence of a central density cusp, we expect rounder, more spherical, models to be closer to integrability and thus to feature more regular orbits. This in turn means that the chaotic effects of introducing a central density cusp are better isolated and therefore more prominently displayed in rounder models. In the case of axisymmetric models, most orbits are regular tubes

whose stability is only reinforced by the central mass concentration.

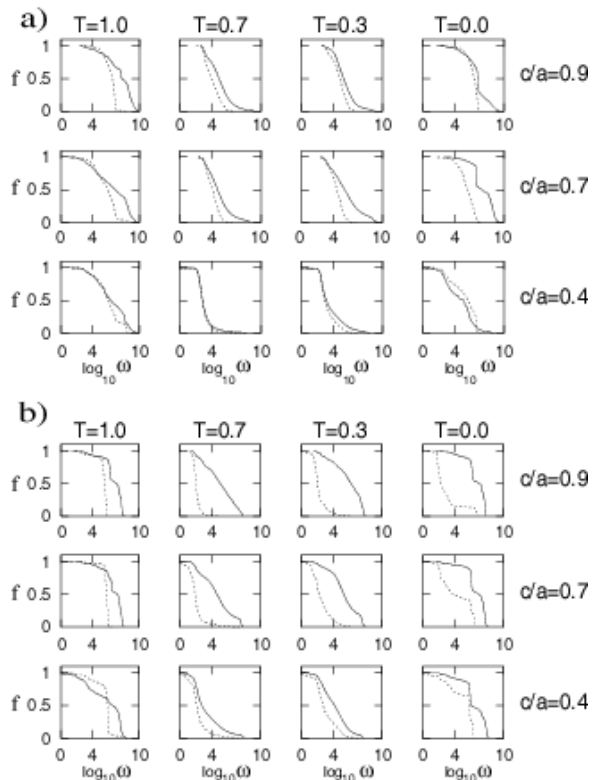


Fig. 5.— Fraction of orbits as a function of the degree of stochasticity for models: a)  $\gamma = 0.5$ , b)  $\gamma = 2$ . Dashed lines represents orbits from the stationary start-spaces, and the full lines orbits from the principal-plane start-spaces.  $\log_{10} \omega = 4$  is the chaotic threshold. Each column represents models with triaxiality  $T = 1.0, 0.7, 0.3, 0.0$  (from left to right) and each row models with long-to-short axis ratios  $c/a = 0.9, 0.7, 0.4$  (top to bottom).

In Figure 6, we analyze the orbital structure of models by graphing the fraction of orbits in each of the four major orbital families: boxes, short axis tubes, long axis tubes and low-order resonant orbits. One drawback of this coarse breakdown is that higher order resonant orbits will be identified as boxes. As expected, bounding axisymmetric models will feature mostly short axis tubes (oblate,  $T = 0$ ) and long axis tubes (prolate,  $T = 1$ ). As the central density cusp is increased,

a roughly even distribution between the boxes, short axis tubes and long axis tubes, present in weak-cusped models only for more spherical cases, expands to include more flattened models with steeper central density cusps. If we recall that box-dominated stationary start-space composes only about 40% of the total number of orbits integrated, it becomes evident that many initial conditions from the principal-plane start-spaces of flatter, weak-cusped models also produce box orbits. The work of Statler (Statler 1987) on building self-consistent models of ‘perfect triaxial galaxies’ which feature smooth cores has evidenced similar behavior to our weak-cusped case; as one moves down the middle of the figure but away from the oblate and prolate limits, the box orbits become progressively more dominant. The reason for this is that, as the mass model becomes elongated in one direction, the tube orbits elongate in the direction normal to it, thus opposing the shape of the mass distribution. This leaves the box orbits as the only ones which can support the triaxial shapes for most models (Statler 1987).

The solutions of the LPP formulation of the Schwarzschild’s method are summarized in Figure 7. For weak cusps, chaotic scattering is less efficient and many regular orbits suitable for reproducing broad ranges of galactic shapes still escape the destabilizing effects of the center. This results in finding self-consistent solutions for all but the most flattened shapes of galaxies with weak central density cusps (Figure 7.a). The non-self-consistency first sets in for flat and nearly prolate models. As the strength of the central cusp is increased, the region of non-self-consistency expands along the prolate boundary (without actually including it) and up the middle of the axis ratio space to include more triaxial models. Eventually, in the case of the strong central density cusp, i.e. the logarithmic scale-free potential, the region of non-self-consistency dominates the entire axis ratio space. It is important to note that the self-consistent region around the oblate edge of the axis ratio space remains fairly large, even when a strong central density cusp is present, while the one around the prolate models remains very thin. This is consistent with the previous findings in which self-consistency prevails only for nearly oblate and prolate models; Figure 1 of (Merritt 1997) shows that for a Jaffe’s density

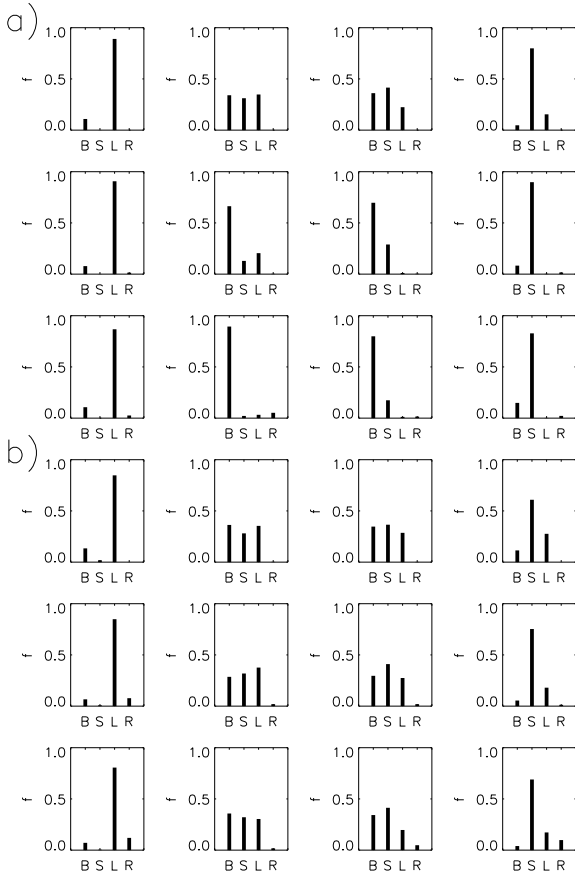


Fig. 6.— Fraction of orbits in each of the five orbital families: B - boxes, S - short axis tubes, L - long axis tubes, R - second and third order resonant orbits. a)  $\gamma = 0.5$ , b)  $\gamma = 2$ . Each column represents models with triaxiality  $T = 1.0, 0.7, 0.3, 0.0$  (from left to right) and each row models with long-to-short axis ratios  $c/a = 0.9, 0.7, 0.4$  (top to bottom).

power law, which behaves as  $\rho \sim r^{-2}$  near the center, i.e. has a strong central density cusp of  $\gamma = 2$ , the self-consistent models are confined to a narrow strip near the prolate boundary and a much thicker region around the oblate boundary. Holley-Bockelmann et al. (2001) used  $N$ -body simulations to construct self-consistent models for a Hernquist  $\gamma = 1$  profile with a range of triaxiality and modest flattening, which is consistent with our Figure 7.b.

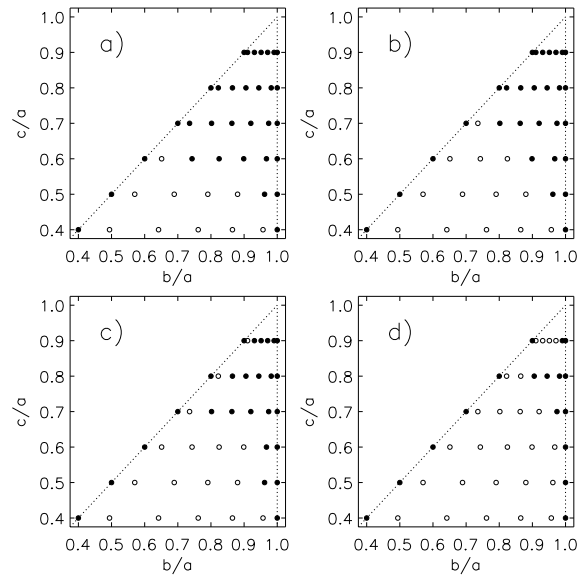


Fig. 7.— Self-consistent ( $\bullet$ ) and non-self-consistent ( $\circ$ ) models for each of the four models: a)  $\gamma = 0.5$ , b)  $\gamma = 1$ , c)  $\gamma = 1.5$ , d)  $\gamma = 2$ .

In order to understand the transition from self-consistency to non-self-consistency, we look at the infeasible cells of the reference sphere, the ones for which constraints (12) are not satisfied. Figure 8 shows the non-feasible cells for each of the models (denoted by dots). As the strength of the central density cusp increases, non-self-consistency is introduced through infeasibility of cells mainly around the short axis ( $z$ -axis) and the  $y$ - $z$  plane. These infeasible regions correspond to chaotic regions of the stationary start-space. Orbits which would reproduce the model's density in those infeasible regions are chaotic and as such averaged into a round super-orbit. We solidify this argument by integrating additional dense population of

orbits in these infeasible regions, which results in most orbits being chaotic, while the regular ones were still not sufficient to reproduce the desired density. This strongly suggests that the chaotic nature of orbits needed to reproduce mass density in those infeasible cells is responsible for the non-self-consistency. However, before any meaningful conclusions about the intrinsic dynamics can be made, one must clearly understand the implications and limitations of the Schwarzschild's method and its dependence on parameters such as the number of orbits integrated, the number of cells of the reference sphere, and the stochastic threshold.

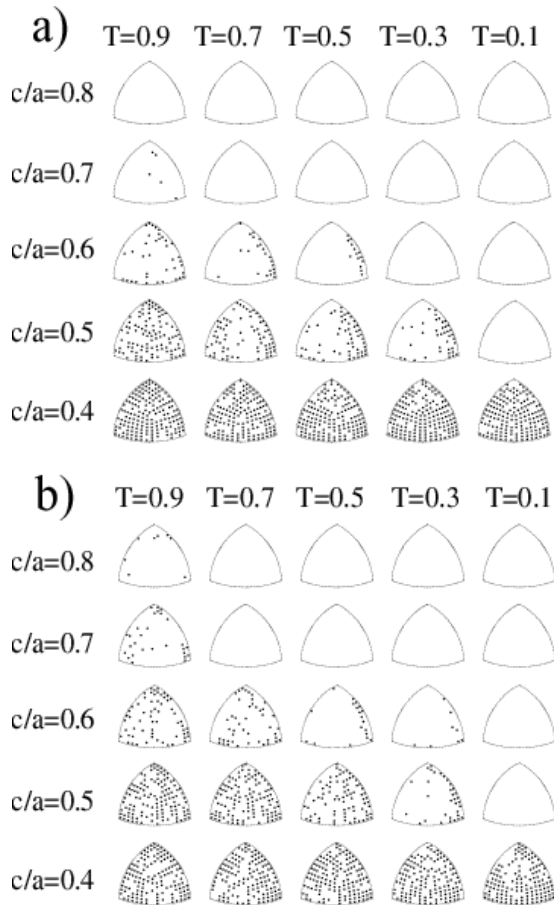


Fig. 8.— Non-feasible cells (marked by dots) for models with a)  $\gamma = 1$  and b)  $\gamma = 1.5$  on a grid of 192 cells.

#### 4.1. Distinguishing Between Numerical Artifacts and Intrinsic Dynamics of the System

As with any numerical model, it is necessary to filter out all of the numerical effects associated with Schwarzschild's method from the underlying dynamics of the system before any physical conclusions are reached. There are two major assumptions and simplifications introduced by Schwarzschild's method. First, the configuration space is *coarse-grained*, divided into cells on which we require the distribution function (DF) to be self-consistent, i.e. to satisfy both the collisionless Boltzmann equation (CBE) and the Poisson equation simultaneously. Second, the system is in equilibrium, i.e. the phase space DF is time-independent.

We probe the coarse-grainedness of the solution by refining the reference grid – we test whether the solutions which are self-consistent on the original grid of 192 cells remain self-consistent when the grid resolution is doubled. The LPP is solved for this finer grid of 384 cells for the  $\gamma = 1.5$  model (Figure 9; compare to Figure 8.b). Only oblate and prolate models remain self-consistent, while other previously self-consistent models fail to satisfy constraints of the optimization problem in several cells. Mathematically, the number of constraints increases with the number of cells, which shrinks the solution space of the LPP and eventually renders the problem infeasible. By the same token, increasing the number of orbital templates increases the number of free variables in the LPP and thus expands the solution space. For non-self-consistent models with 192 cells, increasing the number of orbital templates will not yield self-consistent solutions, which shows that the solutions above reflect true dynamical properties of the model, rather than a numerical artifact. On the other hand, models which are self-consistent on a grid of 192 cells will remain self-consistent if both the number of orbital templates and cells (free variables and constraints, respectively) are increased *simultaneously*. This strongly implies the existence of self-consistent solutions in the continuous limit. We can, therefore, study the effects of central density cusps and galaxy shapes on the true self-consistency (the continuous limit) by studying self-consistency on the discrete grid of 192 cells.

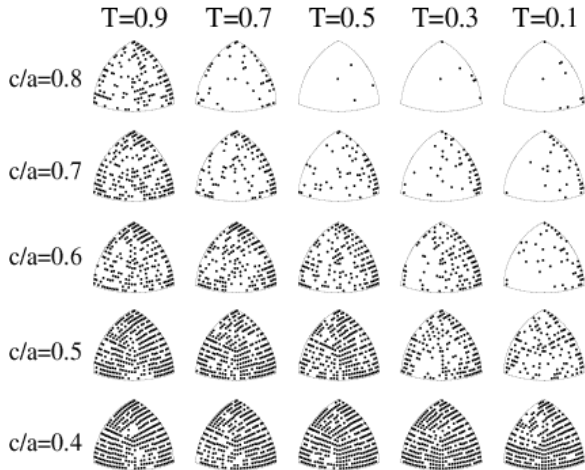


Fig. 9.— Non-feasible cells (marked by dots) for  $\gamma = 1.5$  on a grid of 384 cells.

The integration time of 200 dynamical times was chosen so that the orbital density is well sampled. Such long integration times ensure that most of the ‘sticky’ orbits (Contopoulos 1971; Kandrup, Pogorelov & Sideris 2000; Siopis & Kandrup 2000), which behave as regular for many dynamical times, are detected. If the orbit integration time was any shorter, and the stochasticity criterion not stringent enough to detect such weak stochasticity, many of these orbits would have been included in Schwarzschild’s method as regular, time-independent building blocks. We find that if both regular and chaotic orbits are included into Schwarzschild’s method as time-independent building blocks, self-consistent solutions are readily found for most models (Figure 10, first column). These are non-equilibrium solutions, producing a time-dependent phase space distribution function. Schwarzschild (1993) built several flattened, strongly triaxial, self-consistent models which included chaotic orbits integrated over one Hubble time. Upon integrating orbits from his self-consistent models over three Hubble times instead, the change in orbital densities of the stochastic orbits caused the models to become more round. However, including the time-dependent building blocks in the search for time-independent DFs leads to time-dependent solutions, and violates the initial assumption that the system is in equilibrium. If a numerically ob-

tained DF, a superposition of orbital properties of the library of integrated orbits, undergoes albeit secular changes, the resulting change in model’s mass density gives rise to a different set of orbits. Then the previously computed DF is not a result of a superposition of orbits arising from the changed mass density, and therefore will not be a true self-consistent solution, i.e. will not solve Poisson’s equation and CBE simultaneously. However, in practice it is useful to relax the strict equilibrium requirement, in order to allow those slowly-evolving, quasi-equilibrium solutions to provide us with an insight as to what may happen with self-consistent models in time. Their steady evolution toward more rounder shapes, leads one to suspect that the triaxiality may be a transient feature of elliptical galaxies.

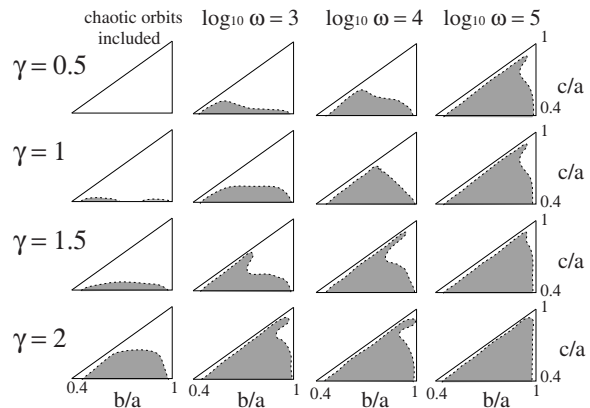


Fig. 10.— Infeasible regions of the axis ratio space (shaded) when chaotic orbits are treated as regular (first column) and for varying values of chaotic threshold  $\omega$ .

It is interesting to observe the dependence of self-consistent solutions on varying the chaotic criterion used to distinguish between regular and chaotic orbits. As the chaotic criterion becomes less restrictive, i.e. as the stochastic threshold  $\omega$  decreases, a larger number of orbital templates are used in the search for self-consistency. Figure 10 demonstrates that as  $\omega$  is decreased, it is possible for a previously non-self-consistent model to attain self-consistency. That is indeed what happens for most non-self-consistent models under consideration. If all orbits are treated as regular

and included in the Schwarzschild’s method, self-consistency is attained for all but the flattest models with strong cusps. On the other hand, if only regular orbits are included (Merritt 1997), or if they are combined with a chaotic super-orbit, the self-consistent regions are significantly limited as we show in this study. This is the consequence of the fact that in flatter and more cuspy potentials, the regular orbits do not have sufficient variety, or, more precisely, do not reproduce the density of the model along the axes. The orbits that would support the prescribed density in these potentials and thus foster self-consistency are rendered chaotic by the scattering effects of the central mass. This points to chaos as the main cause of non-self-consistency. We also observe that as the central density cusp becomes steeper, more centrophilic orbits become chaotic through gravitational scattering of the massive center, thus causing more models to become non-self-consistent through the shortage of regular time-independent orbits which can reproduce the mass density of flattened and triaxial models. It is evident from this that the gravitational scattering by the massive center is the main inducer of chaos.

It has long been known that the solutions to self-consistent problems are highly non-unique (Hunter 1995; Statler 1987; Merritt 1997). Empirically, we see this from the fact that we were able to find as many different DFs as we had cost functions for the LPP problem. Our results show that whenever self-consistent solutions are found, there exists a solution which includes only the regular orbits. Such a solution is found by choosing a cost function for the LPP such as to minimize the chaotic super-orbit. This is, indeed, to be expected, since the orbital density of the chaotic super-orbit is round, and not particularly suitable for reproducing mass density for elongated and strongly triaxial models.

## 5. Discussion and Conclusion

We have studied the effects of central density concentrations on the existence of self-consistent solutions computed using Schwarzschild’s orbit superposition method. The ranges of central density cusps, elongation, and triaxiality, render this analysis comprehensive in its scope. The implementation of the method is described and justi-

fied in detail. Some of its main aspects provide a great deal of information about the dynamics of the system. The start-spaces, stationary and the principal-plane, provide us with a systematic manner in which to sample the phase space and gain an insight about the orbital structure of a given triaxial potential. The classification of orbits based on the leading frequencies in Cartesian coordinates provides us with further information about the orbital structure. Detecting chaotic orbits using a frequency extraction algorithm based on discrete Fourier transforms enables us to distinguish between stochastic and regular orbits. This is essential when it comes to including them in Schwarzschild’s method, since the two are treated differently. We also analyze and discuss in detail the assumptions, implications, and limitations, of Schwarzschild’s orbital superposition method.

The self-consistent solutions obtained through Schwarzschild’s method with chaotic orbits averaged into a super-orbit are equilibrium solutions, since all of their constituents are time-independent building blocks. This time-independence restriction is proven to be the reason why a number of flattened triaxial models are found to be non-self-consistent; some orbits necessary to reproduce model’s elongation and triaxiality are chaotic and thus averaged into a more round super-orbit, causing the mass constraint not to be satisfied. On the other hand, if chaotic orbits are directly included in Schwarzschild’s method, irrespective of the fact that their orbital properties evolve in time, such quasi-equilibrium self-consistent solutions are easily found for most models. This clearly implies that there is no shortage of orbits which could *temporarily* reinforce triaxiality even for time intervals several times longer than the age of the Universe. Truly *permanent* existence depends on the regularity of orbits responsible for reinforcing the prescribed galactic density distribution.

The scale-free property of the potentials investigated here restricts us from knowing directly anything about the self-consistency of models at varying time/length scales. However, it does enable us to isolate the effects of the central density cusp on the global dynamics of the system. Our findings strongly suggest that strengthening the central density cusp increases its ability to scatter centrophilic orbits efficiently and render them chaotic. This is in agreement with earlier stud-

ies of cuspy potentials (Merritt & Fridman 1996; Merritt 1997; Siopis 1999). We also find that this results in increased stability of the centrophobic tube orbits, since for them the strengthening the central density cusp has the effect similar to that of the increase of the central point mass on Keplerian orbits. The breadth of our study, spanning virtually all plausible galactic shapes, elongations, and central densities, shows us how and to what extent triaxiality and central density can cusps coexist. We find self-consistent solutions of weakly-cusped galaxies for almost the entire range of triaxial shapes, while the self-consistent region of the axis-ratio space for strong cusps is limited to nearly axisymmetric, mildly triaxial, regions near the prolate and oblate boundaries.

Our study shows that the gravitational scattering of the massive galactic center is more effective in rendering centrophilic orbits chaotic as the central density cusp becomes stronger. The scattering rids models of regular box-like orbits necessary to reproduce flattened triaxial shapes, thus rendering them non-self-consistent. This establishes gravitational scattering as the key factor in restricting the shapes of elliptical galaxies.

The author is grateful to Christopher Hunter for stimulating discussions, comments, and suggestions. Suggestions by the anonymous referee contributed to the clarity and accuracy of the manuscript. The Florida State University School of Computational Science and Information Technology has been generous in granting access to their supercomputer facilities, which greatly expedited the computations presented here. This study has been supported by the NSF grant DMS-9704615.

## A. Orbital Structure of 2-D Start Spaces

The stationary start-space samples only the positive octant of the equipotential surface. This poses no restrictions on the orbits represented because of the triaxial nature of the potential. Initial conditions are sampled in some systematic fashion over this octant: one can either select the vertices of the equally spaced rectangular grid in each of three regions bounded by planes  $x = y$ ,  $x = z$  and  $y = z$  (Schwarzschild 1993; Merritt & Fridman 1996) or choose centers of equal area segments (Siopis 1999). There is no obvious advantage of one choice over the other.

The principal plane start-space was initially thought of as only an  $x$ - $z$  start-space (Schwarzschild 1993), but was later extended to the other two principal planes so that the symmetries of the system are better respected (Siopis 1999). In both cases, an attempt to minimize duplication of orbits is made by restricting the portion of the principal plane sampled to an elliptical annulus having the equipotential surface as the outer, and the minimum of the amplitudes of the 1:1 periodic thin tube orbits perpendicular to that plane as the inner boundary. The justification of this choice is as follows. Each tube orbit which crosses a given principal plane does so at two points, except in the case of thin tubes, for which the two merge (Statler 1987). Therefore, Schwarzschild argues (Schwarzschild 1993), if one determines the line in the start-space on which thin tubes are located, and if the areas inside these thin tube lines are ignored, one is left with the part of the start-space in which each tube or box orbit is represented by one point (Schwarzschild 1993). This indeed will rid us of the unwanted non-uniqueness of the tube orbits, but it will also eliminate some other non-tube orbits entirely. We illustrate this on the same example as Schwarzschild used to argue his point: an  $x$ - $z$  start-space for the 2-D oblate logarithmic potential with  $c/a = 0.3$  and  $T = 0$  (Schwarzschild 1993, Figure 2).

For 2-D potentials, the  $x$ - $z$  start-space represents *both* stationary and the principal-plane start-space. Each point in the space is a zero-velocity turning point of an orbit at some  $L_z$ , as well as a point at which an orbit pierces the principal plane with velocity component normal to that plane (if one recalls that the magnitude of the  $z$ -component of the angular momentum is given by  $L_z = |x\dot{y} - y\dot{x}|$ ). It may be viewed as a compression of the continuum of surfaces of section: one for each curve of constant  $z$ -component of the angular momentum ( $L_z$ ) (Schwarzschild 1993). Each point on that curve represents an orbit at that angular momentum. A point at which the 1:1 thin tube orbit touches this curve is the boundary which Schwarzschild proposes for the inner boundary of the ellipsoidal annulus. This leaves out all orbits which touch the  $L_z = \text{const.}$  curve *only* at points to the left of this point, such as the 2:3 ‘fish’ orbit, 2:5 and other resonant orbits (Figure 11, top panel). These orbits occupy a non-negligible portion of the phase space, as can be seen from the traditional Poincaré surfaces of section (Figure 11, bottom panel). It is evident from the bottom panel of Figure 11 that the order of the resonance of the boxlet orbit is inversely proportional to the area of the phase space that it occupies.

In order to better understand the structure of orbits on a  $L_z = \text{const.}$  line, we compute the ratios of leading frequencies in  $x$  and  $z$  coordinates for a large number of orbits with initial conditions equally spaced along the curve. Figure 12 shows such ratios for orbits along curves as  $L_z$  is increased. All thick tube orbits are represented by two points, one on each side of the thin tube. Clearly, the ratio of frequencies at such two points is the same, since they both represent the same orbit. Therefore, if the phase space consists only of tubes, the graph of the ratios of leading frequencies should be symmetric with respect to the thin tube location (as in Figure 12.f), albeit with  $x$ -scale somewhat altered. Furthermore, any deviations from such symmetry indicate the presence of resonant non-tube orbits. These resonant orbits are manifested in the graphs of ratios of leading frequencies by sudden jumps and flattenings away from the thin tube. The intersection of the plane in which the Poincaré surface of section is taken with the thick resonant orbit is a set of invariant ‘islands’ surrounding the thin resonant orbit. Our earlier study (Terzić 1998) showed that all of these islands have the same rotation number (defined to be the fraction of a full revolution that an orbit traverses in one iteration around a 1:1 thin tube orbit). Similarly, in the vicinity of a thin orbit, ratios of leading frequencies will be nearly invariant, and appear as flattenings on the curve.

The sequence of Figure 12 clearly reinforces the findings of our earlier studies of axisymmetric scale-free

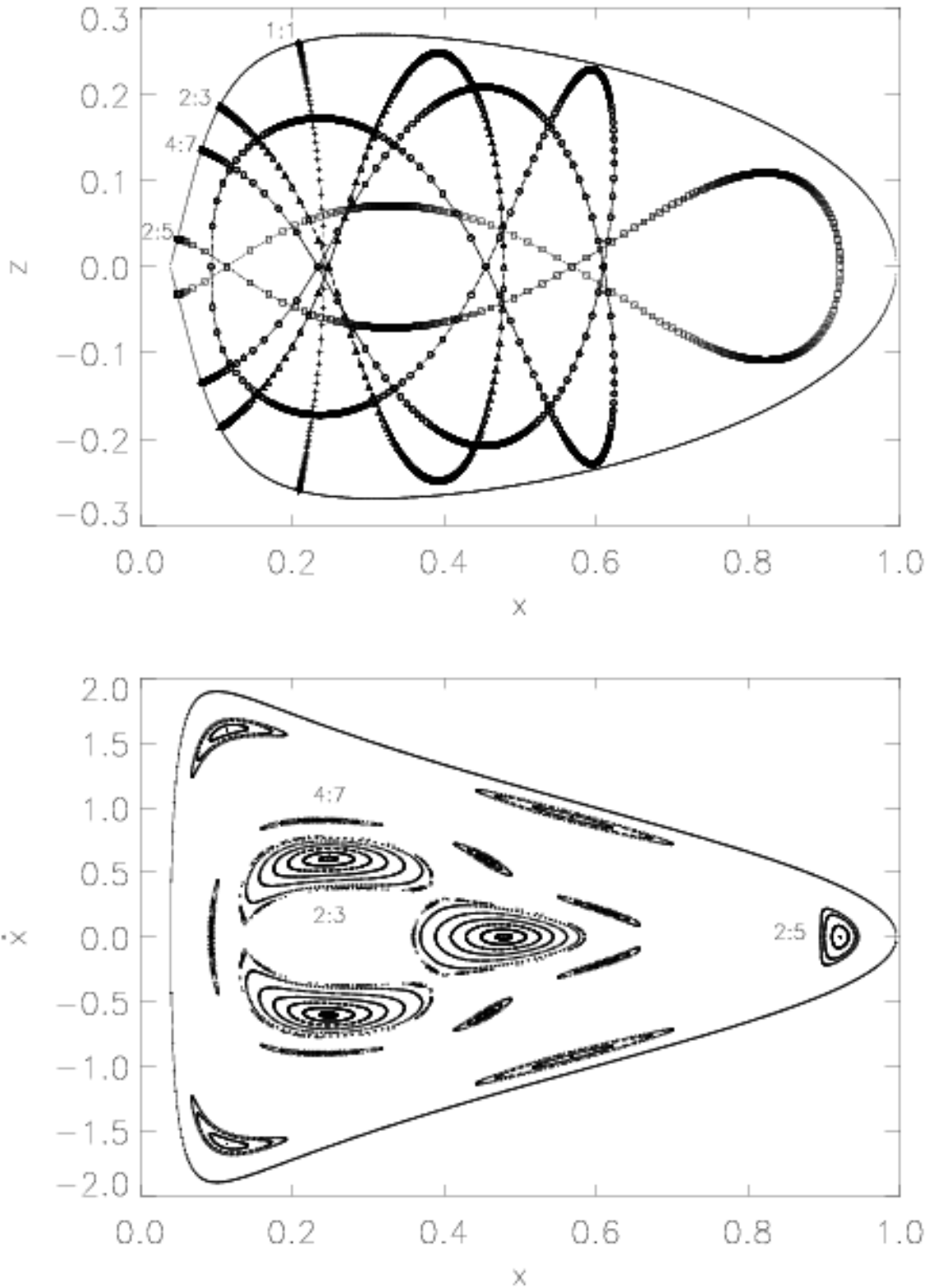


Fig. 11.— **Top:** Some major thin resonant orbits, each representative of an entire family of orbits, originating from points in the  $x$ - $z$  start-space *inside* the radius of the thin tube for the logarithmic potential ( $L_z = 0.1$ ,  $c/a = 0.3$ ,  $T = 0$ ). **Bottom:** Poincaré surface of section for the thick families associated with the thin resonant orbits shown on the left half of the figure. The islands corresponding to the higher order resonances occupy smaller areas.

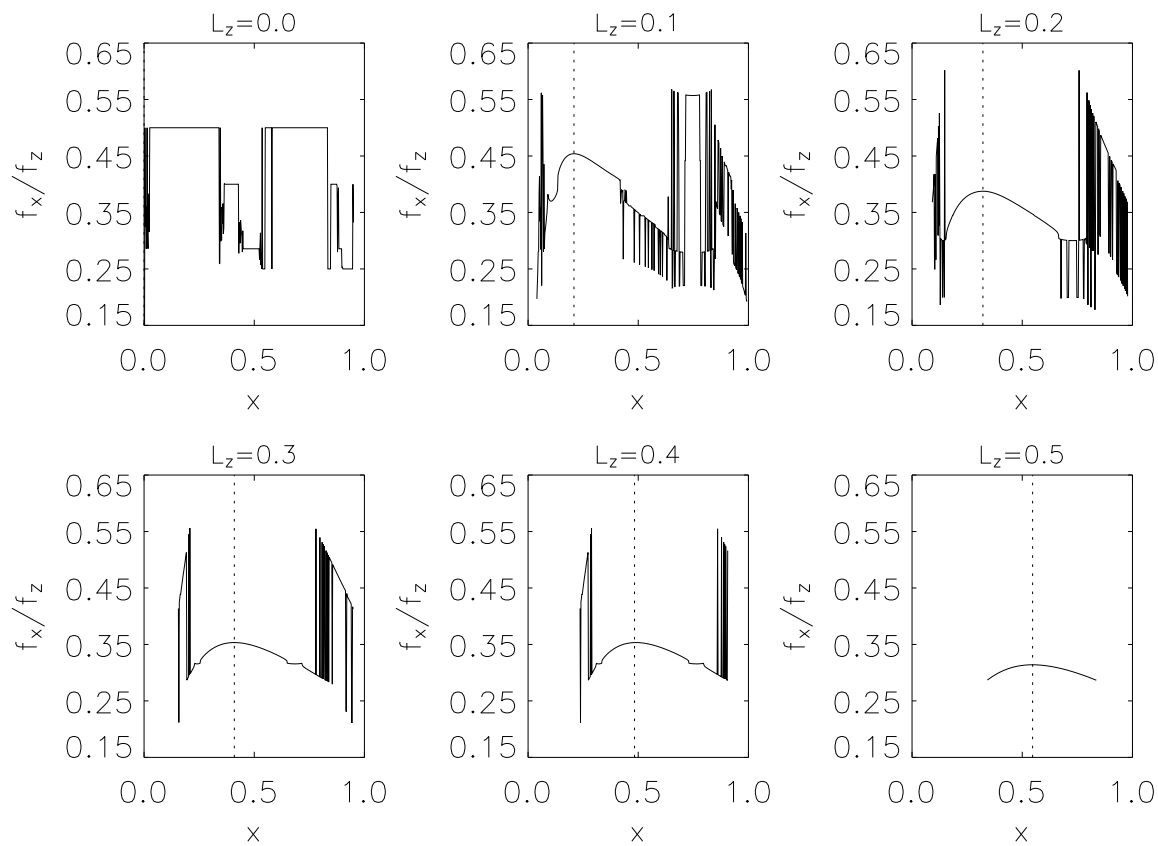


Fig. 12.— Ratios of leading frequencies from the  $x$ - $z$  start-space for a logarithmic potential at varying  $L_z$  values  $L_z = 0, 0.1, 0.2, 0.3, 0.4, 0.5$ . Dashed lines represent the locations of thin tube at that angular momentum. Graphs for higher values of  $L_z$  (up to its maximum of  $L_z = e^{-1/2} = 0.6065$ ) are similar to the graph of  $L_z = 0.5$ , with the domain continually shrinking until it becomes a single point overlapping with the thin tube at the maximum  $L_z$ .

potentials (Hunter et al. 1998) that resonant orbits dominate the phase space at low angular momenta, while the only orbits that remain at large angular momenta are tubes. It is also apparent that most of the resonant orbits bifurcate from the bounding outer planar orbit, while the thin tube becomes unstable only at low angular momenta (Hunter et al. 1998; Terzić 1998). The effectiveness of graphs of ratios of the leading frequencies in identifying the origin of the instabilities makes it beneficial to use them in conjunction with traditional Poincaré surfaces of section in the analysis of phase space and stability.

For triaxial potentials, we divide the duty of sampling the full range of orbits between two 2-D spaces, as outlined above, so that each picks up different types of orbits. The stationary start-space is supposed to select all the resonant orbits with turning points on the equipotential surface. These will not yield any tube orbits, since now  $L_z$  is no longer an integral of motion. The principal plane start-space is three-fold, one in each principal plane. It is designed to pick up tube orbits, but in the process will also pick up resonant orbits which pierce principal planes with velocities normal to the plane (Schwarzschild 1993). Some duplication of orbits is inevitable. If the only goal of the principal-plane start-space is to sample the tube orbits, restricting it to the area outside the thin tube orbit will indeed minimize duplication of tube orbits, *without* systematically leaving out any of them. The same is true of the stationary start-space; if its only goal is to produce the boxes, boxlets and other resonant orbits with zero-velocity turning points, it will indeed do so, albeit with some duplication, without systematically leaving out any orbits. Of course, some minor orbital families may be left out because of the finite resolution of the coverage of these spaces. However, at least theoretically, all tube orbits and orbits with zero-velocity turning points have a chance of being represented, and in the limit of number of points in these spaces  $N \rightarrow \infty$ , they *are* represented. The only remaining question then is whether there exist other families of orbits that this choice of start-spaces systematically leaves out, denying them even a theoretical chance of being represented. One cannot be absolutely definitive in answering this question, but all the empirical indications are that this is not the case, at least not on the level at which it would seriously jeopardize accurate sampling of the phase space.

## REFERENCES

- Binney, J., & Tremaine, S. 1987, *Galactic Dynamics* [Princeton: Princeton University Press]
- Contopoulos, G. 1971, *ApJ*, 76, 147
- Crane, P., Stiavelli, M., King, I. R., Deharveng, J. M., Albrecht, R., Barbieri, C., Blades, J. C., Boksenberg, A., Disney, M. J., Jakobsen, P., Kamperman, T. M., Machetto, F., Mackay, C. D., Paresce, F., Weigelt, G., Baxter, D., Greenfield, P., Jedrzejewski, R., Nota, A., & Sparks, W. B. 1993, *AJ*, 106, 1371
- Cretton, N., de Zeeuw, P. T., van der Marel, R., & Rix, H. 1999, *ApJS*, 124, 383
- Gebhardt, K., Richstone, D., Ajhar, E., Lauer, T., Byun, Y., Kormendy, J., Dressler, A., Faber, S., Grillmair, C., & Tremaine, S. 1996, *AJ*, 112, 105
- Gerhard, O., & Binney, J. 1985, *MNRAS*, 216, 467
- Hairer, E., Norsett, S. P., & Wanner, G. 1993, *Solving ordinary differential equations* [New York: Springer Verlag]
- Holley-Bockelmann, K., Mihos, C., Sigurdsson, S., & Hernquist, L., 2001, *ApJ*, 549, 862
- Hunter, C. 1995, *Annals of the New York Academy of Sciences*, 751, 76
- Hunter, C. 2002, *Space Science Review*, in press
- Hunter, C., Terzić, B., Burns, A., Porchia, D., & Zink, C., 1998, *Annals of the New York Academy of Sciences* 867, 61
- Jalali, A. & de Zeeuw, P. T. 2002, *MNRAS*, 335, 928
- Kandrup, H., Pogorelov, I., & Sideris, I., 2000, *MNRAS*, 311, 719
- Laskar, J. 1993, *Physica D*, 67, 257
- Laskar, J., Froeschlé, C., & Celletti, A. 1992, *Physica D*, 56, 253
- Lauer, T., Ajhar, E., Byun, Y., Dressler, A., Faber, S., Grillmair, C., Kormendy, J., Richstone, D., & Tremaine, S. 1995, *AJ*, 110, 2622
- Levison, H., & Richstone, D. 1987, *ApJ*, 314, 476
- Merritt, D. 1997, *ApJ*, 486, 102
- Merritt, D., & Fridman, T. 1996, *ApJ*, 460, 136
- Mészáros, C. 1996, PhD thesis, Eötvös Loránd University of Sciences
- Moller P., Stiavelli, M., & Zeilinger, W. 1995, *MNRAS*, 276, 979
- Poon, M. Y., & Merritt, D. 2001, *ApJ*, 549, 192
- Richstone, D. 1980, *ApJ*, 238, 103
- Schwarzschild, M. 1979, *ApJ*, 232, 236
- Schwarzschild, M. 1993, *ApJ*, 409, 563
- Siopis, C. 1999, PhD thesis, University of Florida
- Siopis, C., & Kandrup, H., 2000, *MNRAS*, 319, 43
- Statler, T. S. 1987, *ApJ*, 225, 83
- Terzić, B. 1998, *Annals of the New York Academy of Sciences*, 867, 85
- Verolme, E. K. & de Zeeuw, P. T. 2002, *MNRAS*, 331, 959